

# Diameter-Selective Raman Scattering from Vibrational Modes in Carbon Nanotubes

A. M. Rao, E. Richter, Shunji Bandow, Bruce Chase, P. C. Eklund,\* K. A. Williams, S. Fang, K. R. Subbaswamy, M. Menon, A. Thess, R. E. Smalley, G. Dresselhaus, M. S. Dresselhaus

Single wall carbon nanotubes (SWNTs) that are found as close-packed arrays in crystalline ropes have been studied by using Raman scattering techniques with laser excitation wavelengths in the range from 514.5 to 1320 nanometers. Numerous Raman peaks were observed and identified with vibrational modes of armchair symmetry ( $n, n$ ) SWNTs. The Raman spectra are in good agreement with lattice dynamics calculations based on C-C force constants used to fit the two-dimensional, experimental phonon dispersion of a single graphene sheet. Calculated intensities from a nonresonant, bond polarizability model optimized for  $sp^2$  carbon are also in qualitative agreement with the Raman data, although a resonant Raman scattering process is also taking place. This resonance results from the one-dimensional quantum confinement of the electrons in the nanotube.

Since their discovery in 1993 (1, 2), single wall carbon nanotubes (SWNT) have provided the opportunity to study the physical properties of an ordered, one-dimensional (1D) system. Theoretical calculations have shown that, depending on the nanotube symmetry and diameter, these carbon nanotubes can be metallic or semiconducting (3). The electronic and magnetic properties of the metallic tubules have been shown theoretically to be diameter-dependent, and therefore these all-carbon filaments should represent ideal 1D "quantum wires" (3). As we show below, these quantum size effects also manifest themselves in the Raman scattering signal from the nanotube vibrational modes.

Until recently, experimental progress on studying the physical properties of these novel atomic fibers has been slowed because only a minor fraction of the carbons generated in the synthesis process were actually SWNTs [typically, 1 to 4% (1, 2)]. Recent-

ly, a pulsed laser vaporization process was reported that had >70% yield of SWNTs (4), and further improvements in yield have been made (5). We have used a microfiltration technique to remove most of the carbon nanospheres also produced in the process and have isolated nearly pure SWNT samples. In this report, we present results of Raman scattering studies on SWNTs that not only reveal many of the characteristic normal vibrational modes of a carbon nanotube but also show that the Raman excitation frequency can be chosen to excite preferentially nanotubes of a particular diameter for study. Theoretical results are presented in support of the experimental data.

Several Raman (3, 6-9) and infrared (10) studies of multiwall carbon nanotubes (MWNT) (11) have appeared. The larger nanotube diameters and wider diameter distributions inherently present in the MWNTs make it unlikely to observe the nanoscale phenomena that we report. As we show below, the present samples exhibit a very narrow diameter distribution that is populated by only a few distinct tube diameters with the same achiral symmetry. One Raman study on SWNTs has appeared previously (7), in which a spectral subtraction technique was used to remove the contribution from carbon nanospheres, present at ~98 weight % in their sample. In this prior work, a high-frequency Raman doublet was reported that is in good agreement with the present study. However, many new low- and mid-frequency Raman peaks are reported here and their origin is also explained.

Details of the laser-assisted process used to synthesize our SWNTs have appeared elsewhere (4). Briefly, a carbon target containing 1 to 2% Ni/Co catalyst is maintained at 1200°C in a tube furnace and

vaporized by a repetitive sequence of two laser pulses (532 nm, 250 mJ in a 5-mm diameter spot, 10 Hz; and 1064 nm, 300 mJ in a 7-mm diameter Gaussian spot coaxial with the 532-nm laser). SWNTs and, to a much lesser extent, carbon nanospheres are primarily formed in this plasma, and both are swept downstream by flowing argon gas where they are collected on a cold finger before they pass completely out of the furnace. This carbon material (4) was removed and the sample was then soaked in  $CS_2$  to remove fullerenes and other soluble organics. The  $CS_2$ -insoluble matter was then dispersed into distilled  $H_2O$  with 0.1 weight % cationic surfactant (benzalkonium chloride) under ultrasonic agitation to separate carbon nanospheres and catalytic Ni-Co particles from the SWNTs. Microfiltration techniques were then used to isolate the SWNTs from these other solid forms (12). The resultant SWNT carbon material appears in scanning electron microscopy images as a mat of carbon fibers. Under higher magnification in a transmission electron microscope (TEM), a fiber is seen to be a bundle or crystalline "rope" (13) of SWNTs 10 to 20 nm in diameter and ~10 to 100  $\mu m$  in length.

The SWNT diameter distribution for the samples studied was determined from direct measurement of numerous tube widths by using the TEM contrast image when the nanotube or rope bundle was in the focal plane of the microscope. The mean diameter was also determined in this work by x-ray diffraction (XRD). The XRD and TEM (14) probes yielded slightly different values for the mean diameter  $\langle d_t \rangle$ . Values for  $\langle d_t \rangle$  consistent with a (10,10) tube were determined by XRD, in good agreement with a previous XRD study on similar samples (4). However, TEM yielded a  $\langle d_t \rangle$  closer to that of a (9,9) diameter tube. The reasons for this difference are not yet clear. The width of the diameter distribution observed in TEM is consistent with the range of armchair tubes (8,8), (9,9), (10,10), and (11,11).

The notation ( $n, m$ ) defines the atomic coordinates for the 1D unit cell of the nanotube (3). For  $n \neq m \neq 0$ , the tube has chiral symmetry. Achiral tubes exist if  $m = 0$  or  $n = m$ . The former and the latter subclasses of achiral tubes are referred to as "zigzag" ( $n, 0$ ) and "armchair" ( $n, n$ ) tubules. The diameter  $d_t$  for the armchair subclass of SWNTs is linearly proportional to  $n$  and is given by  $d_t(\text{\AA}) = 1.357n$ , where the value  $a = 1.421 \text{\AA}$  has been used for the C-C bond length.

In Fig. 1 we show the Raman spectrum (top) of SWNTs dispersed in a KBr pellet (80 weight % SWNT). All Raman spectra displayed in this report were taken on the

A. M. Rao and P. C. Eklund, Department of Physics and Astronomy and Center for Applied Energy Research, University of Kentucky, Lexington, KY 40506-0055, USA.

E. Richter, K. A. Williams, S. Fang, K. R. Subbaswamy, Department of Physics and Astronomy, University of Kentucky, Lexington, KY 40506-0055, USA.

S. Bandow, Instrument Center, Institute for Molecular Science, Myodaiji, Okazaki 444, Japan.

B. Chase, Dupont Experimental Station, E328163, P.O. Box 80328, Wilmington, DE 19880-0328, USA.

M. Menon, Department of Physics and Astronomy and Center for Computational Sciences, University of Kentucky, Lexington, KY 40506-0055, USA.

A. Thess and R. E. Smalley, Department of Chemistry, Rice University, Houston, TX 77005, USA.

G. Dresselhaus, Francis Bitter Magnet Laboratory, Massachusetts Institute of Technology, Cambridge, MA 02139, USA.

M. S. Dresselhaus, Department of Physics and Department of Electrical Engineering and Computer Science, Massachusetts Institute of Technology, Cambridge, MA 02139, USA.

\*To whom correspondence should be addressed.

same sample that contained microfiltered, randomly oriented SWNTs. The spectra were collected in a backscattering geometry at room temperature with the laser incident at  $\sim 45^\circ$  with respect to the plane of the pellet (15). The spectrum in Fig. 1 was collected by using 514.5-nm excitation and

a spectral slitwidth of  $\sim 2 \text{ cm}^{-1}$ ; the spectrum contains light scattered with the electric vector both parallel and perpendicular to the horizontal plane of incidence. Individual intensity scaling (indicated in parentheses), together with a constant baseline shift, have been carried out for the low-,

mid-, and high-frequency regions of the spectrum to best display all of the Raman features. For clarity, the frequency axis has been expanded in the highest frequency range. Individual Lorentz oscillators are shown below the data superimposed on a flat background and the Lorentzians are intentionally displaced downward for clarity. The bottom of Fig. 1 shows the results of a calculation for the frequency and scattering intensity of the seven strongest Raman-active normal modes of armchair  $(n, n)$  carbon nanotubes, with  $n = 8$  to 11. This range of  $n$  is consistent with the nanotube diameter distribution observed by TEM. Raman-allowed ( $q = 0$ ) phonons were calculated by using C-C force constants optimized (16, 17) to fit the experimental phonon dispersion for a flat graphene sheet. In the present calculations, these same force constants were used to construct the dynamical matrices for each of the  $n = 8$  to 11 armchair nanotubes which were then diagonalized to obtain ( $q = 0$ ) eigenfrequencies and eigenvectors (see Fig. 2) for the Raman-active modes. Theoretical intensities for the SWNT Raman-active vibrational modes were then calculated by using these eigenvectors and a bond polarizability model (18) optimized for other  $sp^2$  carbon materials. The downward-pointing arrows in Fig. 1 indicate the calculated frequencies of the much weaker Raman modes. The calculated frequencies are in good agreement with those obtained previously by a "zone folding" (ZF) model for a flat graphene sheet in which the same force constants were used (17). The predicted diameter dependence of the SWNT mode frequencies can be easily observed in Fig. 1, particularly in the low-frequency region ( $\omega \leq 500 \text{ cm}^{-1}$ ).

The Raman data have been analyzed in terms of armchair symmetry nanotubes for several reasons. First, previous calculations (17) have shown that chiral  $(n, m)$  tubes ( $n \neq m \neq 0$ ) in the diameter region of interest exhibit very few Raman-active modes in the region 400 to  $1500 \text{ cm}^{-1}$ , which is inconsistent with the present observations. If chiral tubes are indeed present, we conclude that they are present in very low concentrations. A similar conclusion was also reached recently in electron diffraction studies of SWNT samples prepared in the same way (19). Of the two remaining symmetry types, zigzag  $(n, 0)$  nanotubes have been found in the ZF model not to exhibit Raman-active modes in the regions from  $650$  to  $770 \text{ cm}^{-1}$  and from  $1400$  to  $1540 \text{ cm}^{-1}$ , and experimental lines were observed at  $673$ ,  $755$ , and  $1526 \text{ cm}^{-1}$ . Although this observation in itself cannot rule out the presence of zigzag tubes in our samples, theoretical calculations of formation energies (20, 21), indicate that  $(n, n)$

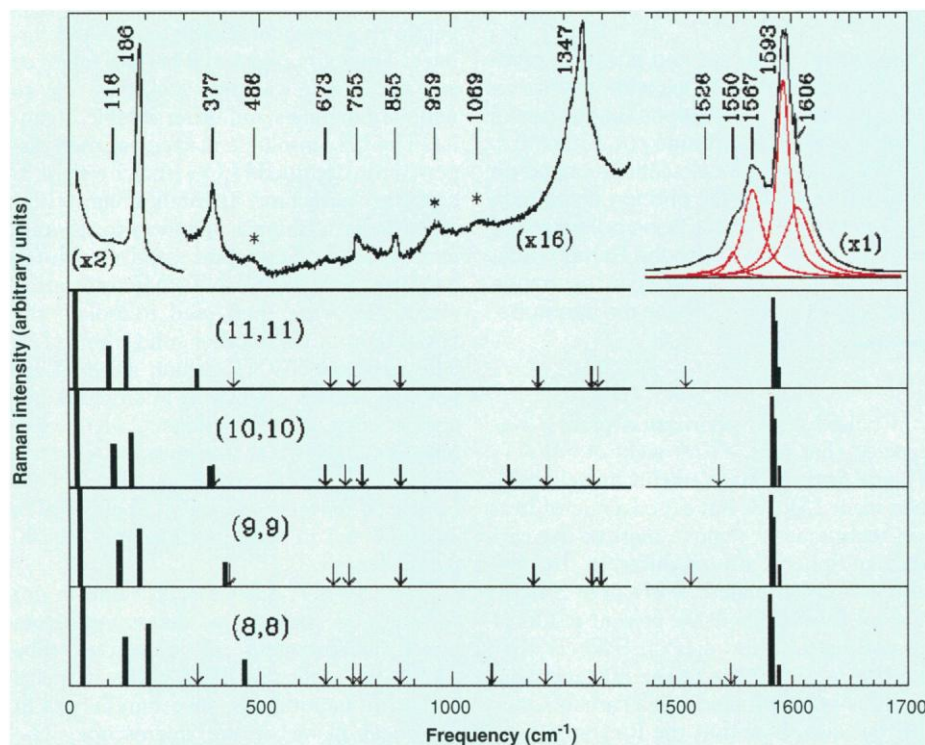


**Fig. 1.** Raman spectrum (top) of SWNT samples taken with 514.5-nm excitation at  $\sim 2 \text{ W/cm}^2$ . The \* in the spectrum indicates features that are tentatively assigned to second-order Raman scattering. The four bottom panels are the calculated Raman spectra for armchair  $(n, n)$  nanotubes,  $n = 8$  to 11. The downward pointing arrows in the lower panels indicate the positions of the remaining weak, Raman-active modes.

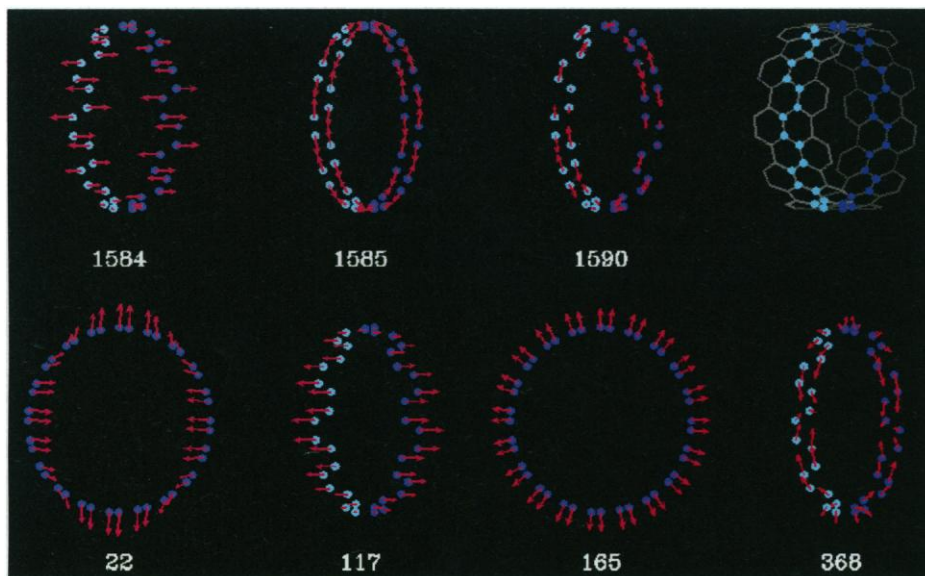


**Fig. 2.** Raman-active normal mode eigenvectors and frequencies for a  $(10,10)$  nanotube. The red arrows indicate the magnitude and direction of the appropriate C-atom displacements, and the eigenvectors shown correspond to the seven most intense modes (see Fig. 1). The unit cell (blue atoms) is shown schematically in the upper right-hand corner.

armchair tubes for  $n = 8$  to 12 are the most stable SWNT species in this diameter range. As we demonstrate below, the Raman scattering data presented here are completely consistent with armchair tubules.

We next discuss the assignment of the peaks in the Raman spectrum at the top of Fig. 1 to specific vibrational modes of  $(n, n)$  SWNTs. The assignments are listed in Table 1 together with the calculated frequencies and symmetry labels for  $n = 8$  to 11 armchair tubes. The assignments are based on the theoretical mode frequencies and intensities shown schematically in Fig. 1. Polarized Raman scattering studies on oriented nanotubes would be needed to further verify the symmetry assignments. At this time, the assignments given here should be considered tentative. In order to simulate the experimental conditions, the calculated intensities shown in Fig. 1 are made for randomly oriented tubes and the appropriate temperature prefactor has been used. Bond polarizability theory (18) predicts seven intense modes, as shown in Fig. 1, and six of these modes were observed. The lowest frequency  $E_{2g}$  symmetry mode, predicted to lie in the range from 18 to 34  $\text{cm}^{-1}$  (Table 1), was not observed because of the large signal from the elastically scattered (Rayleigh) light not rejected by the monochromator. However, the other six modes were detected, although the strongest experimental band centered at 1592  $\text{cm}^{-1}$  is identified with a triplet ( $A_{1g}$ ,  $E_{1g}$ ,  $E_{2g}$ ) of unresolved, intense modes whose frequencies exhibit a weak diameter dependence (Fig. 1 and Table 1). According to theory, there are altogether three possible strong modes in the range from 1581 to 1590  $\text{cm}^{-1}$  associated with each of the four  $n = 8$  to 11 armchair tubes.

Other experimental bands that are predicted by the model to be very weak are nevertheless observed. For the most part, they are indeed observed to be weak, except for the broad feature at 1347  $\text{cm}^{-1}$  which is moderate in intensity (22). It should be pointed out that we expect qualitative, not quantitative, agreement between theory and experiment for the Raman intensities because the bond polarizability model is not expected to perform well at near-resonant scattering conditions.

If we keep in mind that the TEM results indicate that tube diameters in our sample are consistent with an ensemble of (8,8), (9,9), (10,10), and (11,11) tubes, and that the mode frequencies  $\nu(d_t)$  are diameter-dependent, both narrow and broad first-order Raman lines are anticipated on the basis of our calculations. Another example of a broad line is the  $A_{1g}$  symmetry "breathing mode" in which all of the C atoms undergo an equal radial displacement (see

Fig. 2). A strong, broad line is observed with 514.5-nm excitation at 186  $\text{cm}^{-1}$  (Fig. 1). Theory predicts a strong line with a frequency that is strongly diameter-dependent, ranging from 206  $\text{cm}^{-1}$  (8,8) to 150  $\text{cm}^{-1}$  (11,11).

Other mode frequencies exhibit a very weak theoretical  $d_t$ -dependence, and this effect can lead to a narrow first-order band in the experimental spectrum. For example, the feature observed at 855  $\text{cm}^{-1}$  (Fig. 1) is narrow and is identified with the  $E_{2g}$  symmetry vibration that is calculated to be at 866  $\text{cm}^{-1}$  (Table 1) and to be essentially independent of diameter for SWNTs in the range  $n = 8$  to 11. Although inhomogeneous broadening can occur in this ensemble of armchair tubes, the amount of broadening for a specific Raman band depends on the magnitude of the  $d_t$ -dependence of the mode frequency (23). As can be seen from the assignments in Table 1 and inspection of Fig. 1, our phenomenological force constant model is quite successful in predicting mode frequencies for the SWNTs. Clearly the model can be improved, because the force constants used here do not include the effects of the curvature of the tube wall or the redistribution of electrons into 1D band states. Both effects are expected to be most important for the smaller diameter tubes. Our current calculations do demonstrate, however, that force constants appropriate

to a flat graphene sheet can provide a reasonably quantitative phonon model for a SWNT.

We next turn to the dramatic effect of the Raman excitation frequency (wavelength) on the distribution of the intensity and peak positions in the Raman spectrum. In Fig. 3, we display room-temperature Raman spectra for the same sample as a function of laser excitation frequency. The spectra are stacked with the longest wavelength (lowest energy) excitation spectrum on top. From top to bottom, the spectra are collected with the following lasers: Nd:YAG (neodymium yttrium-aluminum-garnet, 1320 nm, 0.94 eV; 1064 nm, 1.17 eV), AlGaAs diode (780 nm, 1.58 eV), krypton (647.1 nm, 1.92 eV), and argon (514.5 nm, 2.41 eV). This excitation range spans the near infrared to the visible. Even a small change in excitation frequency between the 2.41- and 2.54-eV Ar ion laser lines produces dramatic effects on the spectral distribution of the line intensities. Except for the 1.58-eV excited Raman spectrum, there is a shift of intensity toward the lowest frequency modes with increasing laser wavelength until the 1320-nm excitation data, in which scattering from the  $A_{1g}$  breathing mode is also almost extinguished. For example, if we examine the peak intensity of this ~186- $\text{cm}^{-1}$   $A_{1g}$  band measured relative to that of the 1592- $\text{cm}^{-1}$  band, it is observed to be

**Table 1.** First-order Raman-active vibrational mode frequencies in wave numbers for SWNTs. Experimental (514.5-nm excitation; intensity  $I$  is weak, w; moderate, m; or strong, s) and calculated (empirical force constant model). The experimental frequencies vary with laser excitation wavelength (see text and Fig. 3). The SWNT sample is thought to be an ensemble of  $n = 8$  to 11 armchair  $(n, n)$  nanotubes. The mode symmetry (Sym) was determined by model calculations.

Experimental		$n$	Theory				
$\omega_0$	$I$		Sym	(8,8)	(9,9)	(10,10)	(11,11)
			$E_{2g}$	34	27	22	18
116	w	10	$E_{1g}$	146	130	117	106
186	s	8,9,10	$A_{1g}$	206	183	165	150
377 (s)*	m	10	$E_{2g}$	333		368	
377 (b)*	m	9,10	$E_{2g}$	458	408	371	335
			$E_{1g}$		420		431
673	w	8,10	$A_{1g}$	671		670	
			$E_{1g}$		690		683
			$E_{2g}$		732		746
			$E_{2g}$	742		722	
755	w	8,10	$E_{1g}$	762		766	
855	w	8,9,10,11	$E_{2g}$	866	866	866	866
			$E_{2g}$	1106		1152	
			$E_{1g}$		1216		1229
			$A_{1g}$	1247		1252	
1347	m	{ 9,11	$A_{1g}$		1369		1369
		{ 8,10	$E_{1g}$	1377		1374	
1526	w	9,11	$E_{1g}$		1513		1510
1550	m	10	$E_{2g}$			1543	
1567	s	8	$E_{2g}$	1547		1531	
1593	s	{ 8,9,10,11	$A_{1g}$	1583	1584	1585	1586
1609	m	{ 8,9,10,11	$E_{1g}$	1581	1582	1584	1585
		{ 8,9,10,11	$E_{2g}$	1589	1589	1590	1590

\*This line at 377  $\text{cm}^{-1}$  is a superposition of a broad (b) and a sharp (s) peak.

$\sim 1:2.3$  at 514.5-nm (2.41 eV) excitation and  $\sim 2:1$  at 1064-nm (1.17 eV) excitation. At the longest wavelength excitation (1320 nm, 0.94 eV), the intensity ratio is  $\sim 1:20$ . This redistribution in spectral intensity is a clear signal for an unusual resonant Raman scattering process.

Resonant Raman scattering occurs when the energy of the incident photon matches the energy of strong optical absorption electronic transitions (24). We now provide a simple argument that the optical absorption is between electronic states whose character is determined primarily by 1D quantum confinement phenomena. For large enough tube diameter, the character of the electronic states should be essentially independent of tube diameter ( $d_t$ ) or  $n$ , and should therefore closely resemble that of a graphene sheet (3). These larger  $d_t$  tubes would thus not exhibit electronic quantum confinement effects, and a change in the laser frequency would probe nearly identical graphene optical resonances. Therefore, the Raman features for an ensemble of larger diameter nanotubes would be found at the same Raman frequency, independent of the laser excitation frequency, although the relative intensities of these Raman lines might change because of a resonant-scattering process involving graphene-like electronic

states. However, what is observed experimentally for the small diameter nanotubes in our sample are, in many cases, large apparent shifts in the positions of the Raman bands upon variation of the laser excitation frequency. This result indicates that different diameter tubes with different mode frequencies couple with different efficiencies to the laser field. From Table 1, it can be seen that because of the tube diameter dependence, the calculated frequency of the  $A_{1g}$  breathing mode spans the range  $206\text{ cm}^{-1}$  (8,8) to  $150\text{ cm}^{-1}$  (11,11). The peak position of the band identified with the  $A_{1g}$  modes is observed to be  $186\text{ cm}^{-1}$  for 514.5-nm excitation, a few wave numbers greater than the  $183\text{-cm}^{-1}$  value predicted for the (9,9) nanotube. However, at 1064-nm excitation, the  $A_{1g}$  band peak has shifted to  $180\text{ cm}^{-1}$ , a value midway between the  $A_{1g}$  mode frequencies expected for (9,9) and (10,10) nanotubes. At 780-nm excitation, the  $A_{1g}$  band is centered at  $169\text{ cm}^{-1}$ , slightly greater than the value  $165\text{ cm}^{-1}$  predicted for a (10,10) tube, and furthermore, clear shoulders are observed at  $184\text{ cm}^{-1}$  and  $205\text{ cm}^{-1}$ , which are near the breathing mode frequencies predicted for (9,9) and (8,8) nanotubes, respectively (see Table 1). These shifts in position of the experimental Raman features are interpreted as clear evidence for diameter selective coupling of the SWNTs to the exciting radiation field that stems from the  $d_t$ -dependence of the electronic density of states

(DOS) induced by quantum confinement (3). In contrast to this response, although consistent with the explanation given above, is that of the Raman feature at  $\sim 855\text{ cm}^{-1}$  which is experimentally found to be fixed in frequency, independent of the excitation wavelength. As can be seen in Table 1 and Fig. 1, this mode has little or no  $d_t$ -dependence, and is therefore expected to exhibit no frequency shift with excitation wavelength.

In Fig. 4, we show our results for tight binding calculations (25) of the electronic DOS for the  $n = 8$  to 11 armchair tubes under consideration here (Fermi energy  $E_F = 0\text{ eV}$ ). As can be seen in Fig. 4, the DOS for a particular  $(n, n)$  armchair nanotube is the sum of the DOS of 1D electronic bands. As the nanotube diameter increases, the singularities move closer together. For larger diameter tubes whose DOS is not shown in Fig. 4, the singularities merge, become smeared out, and the DOS approaches that of a graphene layer. On the other hand, for small diameter nanotubes as found in the present study, the 1D "spikes" in the electronic DOS are well separated (Fig. 4), especially near  $E_F$ , and can provide initial or final states or both for a highly resonant Raman scattering process.

A near mirror image set of DOS spikes can be observed in Fig. 4; each spike is associated with an  $E^{-1/2}$  singularity characteristic of the dispersion in a 1D electronic energy band (3). Examination of the band structures associated with the DOS indicates that the vertical (momentum conserving) optical transitions that dominate the resonant Raman scattering process occur between mirror image spikes from the valence to conduction band, that is,  $v_1 \rightarrow c_1$  and  $v_2 \rightarrow c_2$  (Fig. 4). As shown in Fig. 4, the characteristic photon energies for these transitions are within the range of most of the laser excitation energies used here [0.94 eV (1320 nm) to 2.41 eV (514.5 nm)]. The observed frequency shifts of the Raman bands with laser wavelength are therefore consistent with the diameter dependence of the DOS peaks of Fig. 4 for an ensemble of  $n = 8$  to 11 armchair nanotubes. As can be appreciated from Fig. 4, resonant scattering from particular diameter  $(n, n)$  tubes will dominate the Raman spectrum when the laser photon energy matches the energy difference between spikes for that  $(n, n)$  DOS. The center of gravity of each Raman band then shifts to the frequency of the  $(n, n)$  vibrational mode being resonantly driven by the laser field. Thus, our observations provide strong evidence for a diameter-selective resonant Raman scattering process that is a direct consequence of the 1D electronic quantum-confinement in small diameter SWNTs.

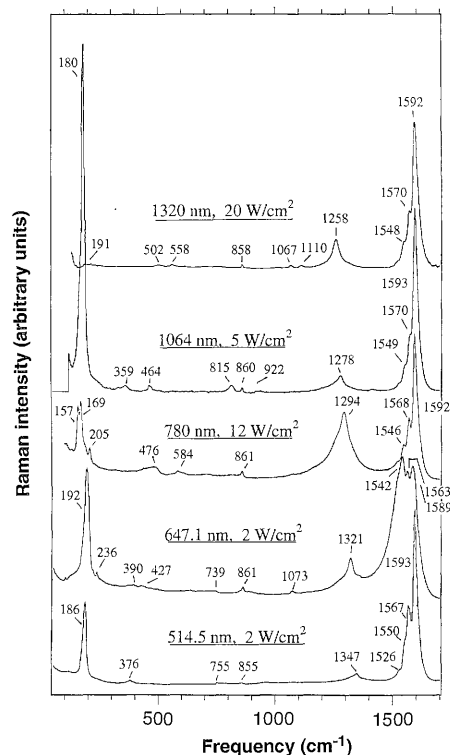


**Fig. 3.** Room-temperature Raman spectra for purified SWNTs excited at five different laser frequencies. The laser frequency and power density for each spectrum is indicated, as are the vibrational frequencies.

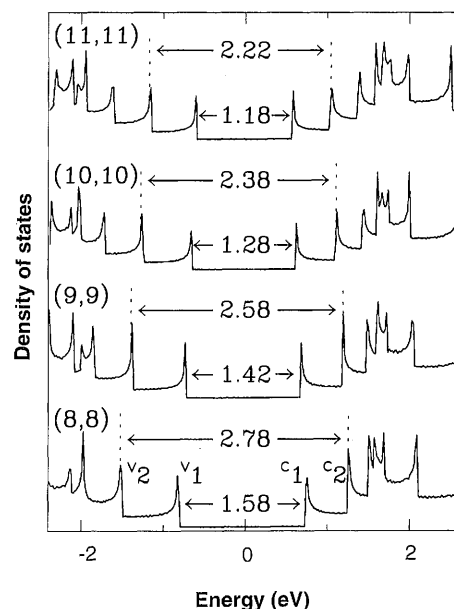


**Fig. 4.** Electronic density of states (DOS) calculated with a tight binding model for (8,8) (9,9), (10,10), and (11,11) armchair nanotubes. The Fermi energy is located at 0 eV. Wave vector-conserving optical transitions can occur between mirror image spikes, that is,  $v_1 \rightarrow c_1$  and  $v_2 \rightarrow c_2$ .

## REFERENCES AND NOTES

- D. S. Bethune *et al.*, *Nature* **363**, 605 (1993).
- S. Iijima and T. Ichihashi, *ibid.*, p. 603.
- M. S. Dresselhaus, G. Dresselhaus, P. C. Eklund, *Science of Fullerenes and Carbon Nanotubes* (Academic Press, New York, 1996).
- A. Thess *et al.*, *Science* **273**, 483 (1996).
- R. E. Smalley *et al.*, unpublished results.
- P. C. Eklund, J. M. Holden, R. A. Jishi, *Carbon* **33**, 959 (1995).
- J. M. Holden *et al.*, *Chem. Phys. Lett.* **220**, 186 (1994).
- H. Hiura, T. W. Ebbesen, K. Tanigaki, H. Takahashi, *ibid.* **202**, 509 (1993).
- N. Chandrabhas *et al.*, *Pramana J. Phys.* **42**, 375 (1994).
- J. Kastner *et al.*, *Chem. Phys. Lett.* **221**, 53 (1994).
- Carbon arc synthesis can also produce MWNTs, which have been shown by TEM to consist of many concentric SWNTs. Each MWNT contains typically between 10 to 20, and as many as 100, concentric tubules with an intertubule spacing of  $\sim 3.4$  Å. A typical inner diameter for a MWNT is  $\sim 8$  nm, a factor of  $\sim 6$  greater than the SWNTs studied here. These MWNTs are too large to exhibit strong quantum-confinement effects, and the Raman spectrum for MWNTs resembles closely that of graphite. See, for example, (6).
- A. M. Rao *et al.*, unpublished results.
- As discussed in (4), the laser-assisted production of SWNTs creates crystalline ropes containing bundles of aligned SWNTs. The tubules stack in a close-packed structure. When viewed end on, the tube ends form a triangular lattice whose lattice parameter has been observed with x-ray and electron diffraction.
- The TEM was calibrated by using the lattice-fringe spacing from graphite (3.35 Å).
- Because the Raman spectra presented in this report were collected with a wide range of laser frequencies, several spectrometers and varying collection optics were needed.
- L. Venkataraman, thesis, Massachusetts Institute of Technology (1993).
- R. A. Jishi, L. Venkataraman, M. S. Dresselhaus, G. Dresselhaus, *Chem. Phys. Lett.* **209**, 77 (1993).
- E. Richter and K. R. Subbaswamy, unpublished results.
- J. M. Cowley, P. Nikolaev, A. Thess, R. E. Smalley, preprint.
- C. H. Xu, C. Z. Wang, C. T. Chan, K. M. Ho, *J. Phys. Cond. Matter* **4**, 6047 (1992).
- Y. H. Lee, M. S. Kim, D. Tománek, private communication.
- Disorder-induced Raman scattering is observed in many forms of  $sp^2$  carbon. The width of the  $1347\text{-cm}^{-1}$  peak is narrow relative to that typically seen in these other  $sp^2$  carbons. Furthermore, we observe a large downshift of more than  $177\ 100\text{ cm}^{-1}$  for this band with decreasing excitation frequency (see Fig. 3), which has not been reported previously for other  $sp^2$  carbons.
- Strictly speaking, the concept of a diameter-dependent shift in mode frequency should be applied separately to  $n = \text{even}$  and  $n = \text{odd}$  tubes, because some of the mode frequencies show an abrupt change in frequency as  $n$  changes by one (that is,  $n = \text{even}$  to  $n = \text{odd}$ ), consistent with the different symmetry groups that are applicable to even and odd tubes.
- W. Hayes and R. A. Loudon, *Light Scattering by Crystals* (Wiley, New York, 1978).
- M. Menon, E. Richter, K. R. Subbaswamy, *J. Chem. Phys.* **104**, 5875 (1996).
- The Kentucky group was supported by the University of Kentucky Center for Applied Energy Research and NSF grant OSR-94-52895 and DOE contract DE-F22-90PC90029. The MIT authors gratefully acknowledge NSF grant DMR95-10093 for support of this research. The work at Rice was supported by the Office of Naval Research contract N0014-91-J1794. The work at IMS was supported by the Grant-in-Aid for Scientific Research (C) 08640749 from the Japanese Ministry of Education, Science, Sports, & Culture.

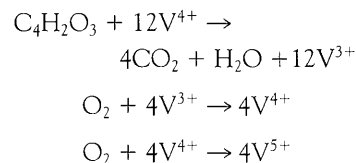
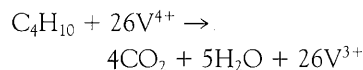
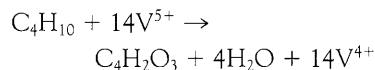
28 October 1996; accepted 19 December 1996

# The Kinetic Significance of $V^{5+}$ in *n*-Butane Oxidation Catalyzed by Vanadium Phosphates

George W. Coulston,\* Simon R. Bare, Harold Kung, Kari Birkeland,† Gregory K. Bethke, Richard Harlow, Norman Herron, Peter L. Lee

Maleic anhydride, a precursor to polyester resins, is made by oxidation of *n*-butane over vanadium phosphate catalysts. This system is of general interest because it is the only heterogeneously catalyzed, alkane-selective oxidation reaction in commercial use. Time-resolved in situ x-ray absorption spectroscopy shows that when either  $\alpha_1\text{-VOPO}_4/\text{SiO}_2$  or  $(\text{VO})_2\text{P}_2\text{O}_7/\text{SiO}_2$  catalysts are exposed to *n*-butane, the rate of maleic anhydride formation is proportional to the rate of decay of  $V^{5+}$  species in the catalyst. Thus  $V^{5+}$  species are kinetically significant for the production of maleic anhydride and not just for the production of by-products. The results also suggest that  $V^{5+}$  species may play a role in the initial hydrogen abstraction from *n*-butane, the rate-determining step in the reaction sequence.  $V^{4+}$  sites appear to be responsible for by-product formation.

Conversion of *n*-butane to maleic anhydride, an important raw material used in polyester resin production (1), is the only heterogeneously catalyzed, alkane-selective oxidation reaction in commercial use. This oxide system has generated widespread interest because better understanding of the structure-property relations in the vanadium phosphate (VPO) family of materials could promote development of other selective oxidation processes. Selective oxidation reactions on reducible metal oxides are generally believed to follow the Mars and van Krevelen (2) mechanism. The metal oxide participates in a series of redox steps: Oxidation of an adsorbed organic molecule first reduces the metal cation, which is subsequently reoxidized either directly by gas-phase oxygen or by oxygen that has diffused through the lattice of the catalyst. At steady state, the oxide typically contains metal cations in different oxidation states, and each state plays a different role in the reaction mechanism. For the case of *n*-butane oxidation over VPOs, Bej and Rao (3) proposed a mechanism based on the following set of reaction steps:



The above mechanism is grossly oversimplified not only because it ignores many of the intermediates produced during *n*-butane partial oxidation to maleic anhydride (4–6), but also because it is not formulated with elementary reaction steps. In any case, inferring structure-performance relations based on gas-phase kinetics alone is problematic because the catalyst kinetics have not been determined.

The only detectable crystalline phase in aged industrial catalysts is vanadyl pyrophosphate,  $(\text{VO})_2\text{P}_2\text{O}_7$  (7), which contains  $V^{4+}$  cations. Nevertheless,  $\text{VOPO}_4$  ( $V^{5+}$ ) phases have been observed in working catalysts through in situ laser Raman studies (8, 9). Several authors (3, 10–12) have speculated on the role of  $V^{5+}$  centers in maleic anhydride production. Others have attributed significance to shear steps formed at the surface of  $(\text{VO})_2\text{P}_2\text{O}_7$  upon exposure of the catalyst to *n*-butane (13). However, in situ catalyst characterization under steady-state conditions, even when combined with reaction product analyses, is insufficient to establish the kinetic significance of an observed species. To claim a species is kinetically significant, it must at least be shown to react with a rate sufficient to support the overall rate of reaction (14). Such experiments require in situ monitoring of the oxide catalyst with a technique that is both fast ( $\sim 1$  s) and quantitative. In situ, dispersive time-resolved x-ray absorption spectroscopy (TRXAS) meets both of these criteria. In this report, we describe our approach, which combines dispersive

G. W. Coulston, R. Harlow, N. Herron, DuPont Company, Wilmington, DE 19880-0262, USA.

S. R. Bare, Dow Chemical Company, Midland, MI 48674, USA.

H. Kung, K. Birkeland, G. K. Bethke, Ipatieff Laboratory, Northwestern University, Evanston, IL 60208-3000, USA.

P. L. Lee, Materials Science Division, Argonne National Laboratory, Argonne, IL 60439, USA.

\*To whom correspondence should be addressed.

†Present address, Dow Chemical Company, Midland, MI 48674, USA.